

Can A Neural Network Hear the Shape of A Drum?

Y. Zhao and M.M. Fogler

Department of Physics, University of California San Diego, 9500 Gilman Dr, La Jolla, CA 92093

Abstract

We have developed a deep neural network that reconstructs the shape of a polygonal domain given the first hundred of its Laplacian (or Schrodinger) eigenvalues. Having an encoder-decoder structure, the network maps input spectra to a latent space and then predicts the discretized image of the domain on a square grid. We tested this network on randomly generated pentagons. The prediction accuracy is high and the predictions obey the Laplacian scaling rule. The network recovers the continuous rotational degree of freedom beyond the symmetry of the grid. The variation of the latent variables under the scaling transformation shows they are strongly correlated with Weyl’s parameters (area, perimeter, and a certain function of the angles) of the test polygons.

The title of this paper is a reference to a famous question “Can One Hear the Shape of a Drum?” [1]; that is, whether any two isospectral planar domains are necessarily isometric. Strictly speaking, the answer is negative; however, the known counter-examples [2] are rare and generally presumed to be of measure zero [3,4]. In other words, the answer is affirmative for a vast majority of shapes [5–10]. The natural follow-up question is to how to reconstruct the shape of the domain from its spectrum, i.e., from a handful of its first Dirichlet eigenvalues. We call this inverse Dirichlet problem or IDP. Existing numerical algorithms solve the IDP by iterative morphing of the embedding mesh until the eigenvalues match those of the true ground [11,12]. This method is computationally intensive and its convergence often depends on a good initial guess.

In recent years, deep neural networks (DNN) have gained popularity as a new tool for solving a variety of inverse problems. In physical science, examples include optimization of photonic crystals, [13] data analysis in microscopy and spectroscopy, [14,15] detection of quantum phases, [16–18] and subatomic particles in collision experiments. [19–21] Some studies in computer vision used DNN to solve problems conceptually similar to IDP, e.g., reconstruction of 3D geometries from 2D images or 1D vector encodings [22–25] and 2D images from text descriptions [26–28]. It is therefore may be expected that the DNN is capable of solving the IDP, at least for certain classes of 2D shapes.

In this work, we present a proof-of-principle demonstration that DNN can accurately solve the IDP for randomly generated pentagons. Additionally, we attempt to examine the properties of the function learned by this DNN. We find evidence that the DNN discovered the scaling laws of the Laplace operator and the rotational symmetry of the problem. We also find a strong correspondence between the latent variables of the DNN and the three Weyl parameters (area \mathcal{A} , perimeter \mathcal{L} , and a certain function \mathcal{K} of the angles, see below).

We now describe the data generation and the structure of our DNN. The vertices of the pentagons were generated in polar coordinates with polar distances uniformly sampled between 0.5 and 2. To ensure the proper size of the pentagons, the corresponding polar angles were generated such that the included angles between neighboring radii have values between $\pi/10$ and π . The associated first 100 Dirichlet eigenvalues were calculated using a standard finite-element solver (Mathematica). It is important to notice that the computed eigenvalue spectrum is invariant under any translations, rotations, and reflections of the underlying shape. However, in IDP these isometric transformations would introduce ambiguity in the DNN output. To eliminate this “gauge freedom,” we did the following. First, we shifted the centroids of the pentagons to the origin. Second, we rotated the pentagons such that the vertex with the smallest inner angle is located on the positive x -axis. Finally, the remaining reflection symmetry was integrated into the loss function to be discussed later in this section. After the above procedure, the chosen representations were coarse-grained into 41×41 binary images I_{true} by dividing the square $-2 \leq x, y \leq 2$ into pixels of size 0.1×0.1 . For these input images we restricted the pixel values to be binary, $p_i = 0$ or 1. On the other hand, the output of the DNN are images I_{pred} that we allowed to have fractional pixel values $0 \leq q_i \leq 1$.

To quantify the similarity between the predicted and the original images we used the Jaccard index (sometimes called the IoU index), which is defined as the ratio between the intersection (I) and the union (U) of two sets. In our case, the Jaccard index $J(I_{\text{pred}}, I_{\text{true}})$ takes the form

$$J(I_{\text{pred}}, I_{\text{true}}) = \frac{\sum_i p_i q_i}{\sum_i p_i^2 + q_i^2 - p_i q_i}. \quad (1)$$

Here the summation index i runs over the entire 41×41 image. The Jaccard index is a number between zero and one, the latter being reached if the images are identical, $p_i = q_i$. To combat the aforementioned “gauge freedom” problem, we chose the loss function L to be

$$L = \min_{\pi \in D_4} [1 - J(\pi(I_{\text{pred}}), I_{\text{true}})], \quad (2)$$

where π is an element in the dihedral group D_4 which describes the symmetry of a square.

Our DNN has the encoder-decoder structure. Networks with such a structure have been shown to handle many complicated tasks including detecting abnormal quantum phases, [29] approximating quantum state distributions, [30] and parametrizing nonlinear dynamics [31–33]. Recent studies have also shown that encoder-decoder DNNs have the ability to discover key physical parameters of the problem [34,35]. As depicted in Fig. 1, the input to the DNN consists of the first 100 eigenvalue spacings. The encoder portion is composed of three consecutive long-short term memory (LSTM) [36] layers of size 128 each. The latent layer directly after the encoder contains 10 neurons with linear activation. It is crucial to notice that even though seven independent parameters are enough to uniquely determine a pentagon, we still expand the latent space to increase the DNN approximation capability. The decoder starts with four dense layers of sizes 50, 512, 1024, and 3200 with LeakyReLU activation (negative slope coefficient set to 0.3 and is the same for the rest of this section). [37] Next, the output vector of size 3,200 is reshaped to 128 images each of size 5×5 . Four Transpose Convolution layers with kernel sizes 64, 32, 16,

and 1, then up-samples the 5×5 images to the final prediction of size 41×41 . The first three Transpose Convolution layers have the ReLu activation while the last one has sigmoid activation to constraint the predicted pixel values. During training, the loss function defined in Equation (2) is applied and 20% of the samples are used for validation. A total of 1,100,000 training samples are fed into the network in 11 batches. The training epoch number for each batch decreases linearly from 50 to 10. We used the Adam optimization method with an initial learning rate of 10^{-3} and a decay rate of 10^{-5} . After training, a test data set containing 100,000 new samples was used to measure the prediction accuracy

Our results are demonstrated in Fig. 2 where we present the cumulative distribution function (CDF) of the Jaccard index loss L for the test dataset. For almost all testing samples, the loss function produces values below 0.5. The mean of the entire distribution occurs at 0.069 and only 33% of the total cases have losses larger than that. To illustrate the relation between the value of the Jaccard index and the visual goodness of the DNN predictions, we provide three examples marked “good”, “mediocre,” and “bad”, which correspond to the top 15%, mid 70%, and the bottom 10% of the CDF, respectively. The “good” prediction captures almost every detail of the true polygonal shape (boxed in red, same for other examples), with sharp boundary and only a few pixel-level discrepancies present. In the “average” prediction, the perimeter become blurry. The major inconsistency is seen in the upper right vertex separated by a dashed blue line: this structure is missing in the prediction; however, a similar shaped triangle appears on an adjacent edge. We will discuss a possible reason for this misconstruction later in this section. In the example of a “bad” prediction, only one vertex appears sharply defined while the remaining ones become smeared. We think that these failures resulted from the rareness of such instances in the training set. Overall, since our DNN captures the true geometry of the boundaries for the majority of the tested samples, we conclude that it can indeed “hear” the shape of a pentagon from its overtones.

Next, we address the question whether the DNN is capable of learning basic properties of the Dirichlet problem. We attempt to answer this question by investigating the scaling behavior of the DNN output. For example, the magnitude of the eigenvalues scales inversely proportional to the square of the linear dimension of the drum. Therefore, scaling of the DNN input (level spacings) by a factor of S should make the predicted area \mathcal{A} expand by a factor of $1/S$. To check if the DNN adheres to this rule, we repeated the simulations applying scaling factors $0.5 \leq S \leq 2.5$ to the previous dataset. The results are demonstrated in Fig. 3. In Fig. 3(a) we show the scaling behavior of a typical “good” prediction. For this example, the predicted polygons vary in size according to the expected scaling rule. All major features of the drum boundary are maintained in both enlarged and shrunken images. Surprisingly, the same scaling rule is also exhibited by the “bad” prediction. As demonstrated in Fig. 3(b), the DNN not only correctly boosts this faulty prediction but it also preserves all its major features. To check the area scaling quantitatively, we defined the area \mathcal{A} of the predicted pentagon to be the sum of all the pixel values. We observed that it has a power-law dependence on the eigenvalue scaling factor S with the exponent of -0.93 , which is very close to the expected -1 , see Fig. 3(c).

Another surprise is that the DNN also discovers the continuous rotational degree of freedom beyond the symmetry of the underlying square grid. As exemplified in Fig. 4, after a

counterclockwise rotation of 150° , a seemingly fallacious prediction with $L = 0.35$ shows a much better agreement with the true ground ($L = 0.13$). Such cases make up roughly one third of the worst 20% of all the predictions. Additional examples of seemingly “bad” predictions include instances where L can be greatly reduced if a suitable rotation is combined with a reflection, see Fig. S1 in the supplementary material. It is remarkable that these predictions exist despite being penalized by the loss function. They suggest that the DNN must have captured fundamental information associated with the geometry of the drumheads.

Frequently discussed in the context of the IDP is Weyl’s formula [3,38,39] for the average number of eigenvalues below a prescribed value E :

$$\bar{N}(E) \simeq \frac{\mathcal{A}}{4\pi} E - \frac{\mathcal{L}}{4\pi} \sqrt{E} + \mathcal{K}. \quad (3)$$

Here \mathcal{L} is the perimeter of the polygon, constant \mathcal{K} is given by

$$\mathcal{K} = \frac{1}{24} \sum_i \left(\frac{\pi}{\alpha_i} - \frac{\alpha_i}{\pi} \right), \quad (4)$$

and $0 < \alpha_i < 2\pi$ are the inner angles. We find evidence that the DNN discovers Weyl’s expansion and stores information about the three parameters $\mathcal{A}/4\pi$, $\mathcal{L}/4\pi$, and \mathcal{K} in the latent neurons. To do so we utilize the universal approximation property [40] of neural networks to establish a mapping from the latent neurons to Weyl’s parameters. Specifically, we detached the encoder and the latent layer from the original DNN and connected it instead to another small network whose outputs were Weyl’s parameters (or other parameters of interest, see below). To control the complexity of the mapping function, we varied the number of hidden layers in the small network but fixed the size of each layer to 50 neurons, see Fig. 5(a). We kept the output layer activation-free and hence the only source of nonlinearity in the small network was the hidden layers where the LeakyReLU activation function was applied. During training, we allowed modifications of the small network parameters only, using the mean squared error (MSE) as the loss function. In a similar way, we constructed two other networks, one predicting Cartesian coordinates of the polygon vertices and another one predicting the edge lengths and inner angles of the polygons. These more traditional ways to define shapes were included for comparison.

We used 1,100,000 samples to train the mapping from the latent space to each of these three sets of boundary descriptors. The testing results from 100,000 samples are demonstrated in Fig. 5(b), where the mean predicted percentage errors for every parameter set are graphed as functions of the number of the hidden layers. Notably, for Weyl’s parameters, the error is as low as 6% for a simple linear mapping. When nonlinearity is later introduced, the error plateaus at 1.8%. In contrast, even equipped with the highest level of nonlinearity, the network struggles to construct the mapping functions for the remaining two sets of the descriptors. The prediction accuracies hardly surpass those of random guess. We conclude that the latent representation has the closest relation to Weyl’s parameters.

At this point it still remains a question whether the combined network understands the meaning of \mathcal{A} , \mathcal{L} , and \mathcal{K} . Since no additional physical information, e.g., measurement units, was provided

during training, it is possible that the learned mapping treated the Weyl’s parameters as unitless and hence overfitted them. To check if that is the case we again investigated the scaling behavior of the outputs. Unlike the DNN predictions of the images, the output Weyl’s parameters should obey different scaling laws: \mathcal{A} should scale as $1/S$, \mathcal{L} as $1/\sqrt{S}$, while \mathcal{K} should be scale-invariant. As demonstrated in Fig. 6, for a network with one hidden layer, the average \mathcal{A} , \mathcal{L} , and \mathcal{K} predictions indeed follow the correct scaling laws. In this Figure we included only the samples and scaling factors S for which the scaled shapes remain within the training range (for the entire data set, see Fig. S2 in the Supplementary materials). From the above results, we confirm that Weyl’s parameters are stored in the latent space quasi-linearly, and so the prediction of the drum shapes by the encoder-decoder network may be aided by these parameters. Yet another evidence in favor of this interpretation is obtained by analyzing the “mediocre” prediction from Fig. 2. This prediction misses the upper right corner of the pentagon, as outlined by the green line in Fig. 7 but includes an extra triangular region traced by the blue line. These two regions, the missing one and the added one, are approximately isometric, and so the predicted image preserves Weyl’s parameters of the true ground.

In conclusion, we have developed an encoder-decoder DNN that solves the IDP for simple shapes such as pentagons with an exceptional accuracy. We presented evidence that this DNN has learned the scaling properties of the Laplacian operator and that it stores information about Weyl’s expansion parameters (area \mathcal{A} , perimeter \mathcal{L} , and inner-angle characteristic \mathcal{K}) in the latent representation. The DNN has discovered a continuous rotational symmetry of the Dirichlet problem beyond the limitations of the square grid. Note that the latent space must also contain information about other boundary descriptors, such as the Cartesian coordinates of the vertices. However, we found extracting these more readily interpretable parameters challenging. We think that by implementing a mutually independent latent space [34] and more extensive training, one could potentially do so as well. Another possible extension of the present work is to consider non-polygonal, e.g., smooth shapes.

Our study was originally motivated by scanning probe optical nanoscopy, where the methods developed to tackle IDP could help to achieve super-resolution of the shapes of nanoparticles using their collective mode spectra [41]. We hope our work would stimulate applications of DNN to solving inverse spectral problems in this and various other fields.

Note added. When this paper has been completed, we learned of a related work [42] where the DNN was successfully applied to solving the IDP for 3D shapes representing human facial expressions. That work was motivated by industrial applications of computer vision techniques. No attempt to analyze the physical and mathematical properties of the latent variables was made.

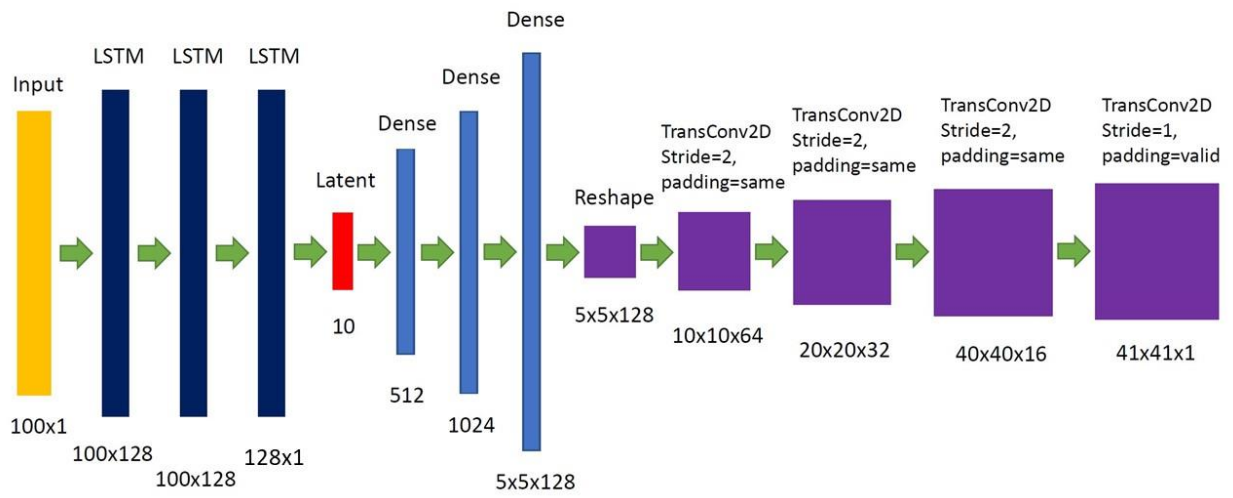


FIG 1. Structure of the DNN containing an encoder, a latent layer, and a decoder. The encoder consists of three consecutive LSTM layers. The decoder first expands the latent space via three dense layers, then reshapes the result, then decodes the image using four 2D transpose convolutional layers.

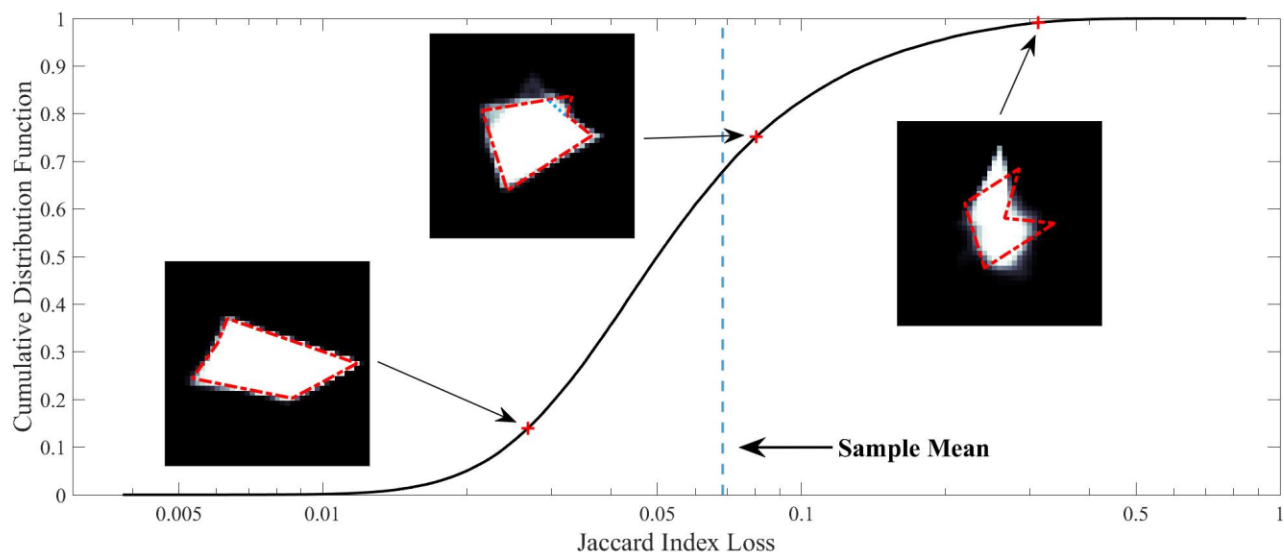
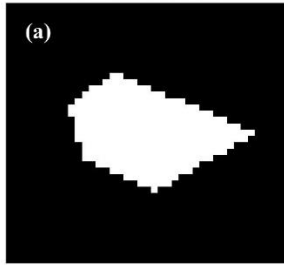
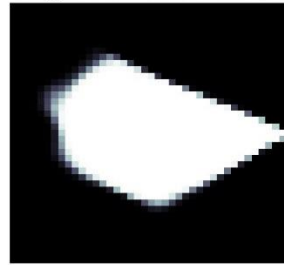


FIG 2. Cumulative Distribution Function (CDF) of the Jaccard Index (IoU) loss for a test dataset containing 100,000 samples. The dashed vertical line indicates the sample mean. The three red crosses mark typical “good”, “mediocre,” and “bad” predictions. The dashed red boxes indicate the true ground.

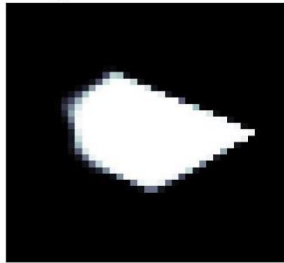
True Ground



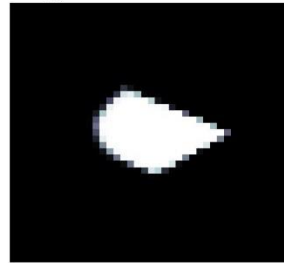
Eigenvalue Scale = 0.6



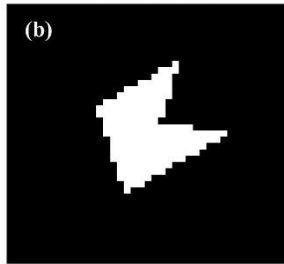
Eigenvalue Scale = 1



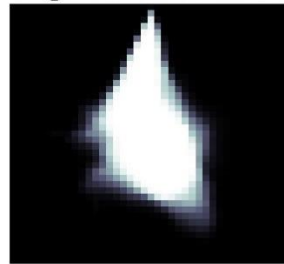
Eigenvalue Scale = 2.0



True Ground



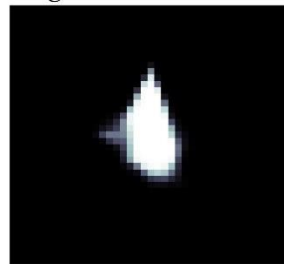
Eigenvalue Scale = 0.6



Eigenvalue Scale = 1



Eigenvalue Scale = 2.0



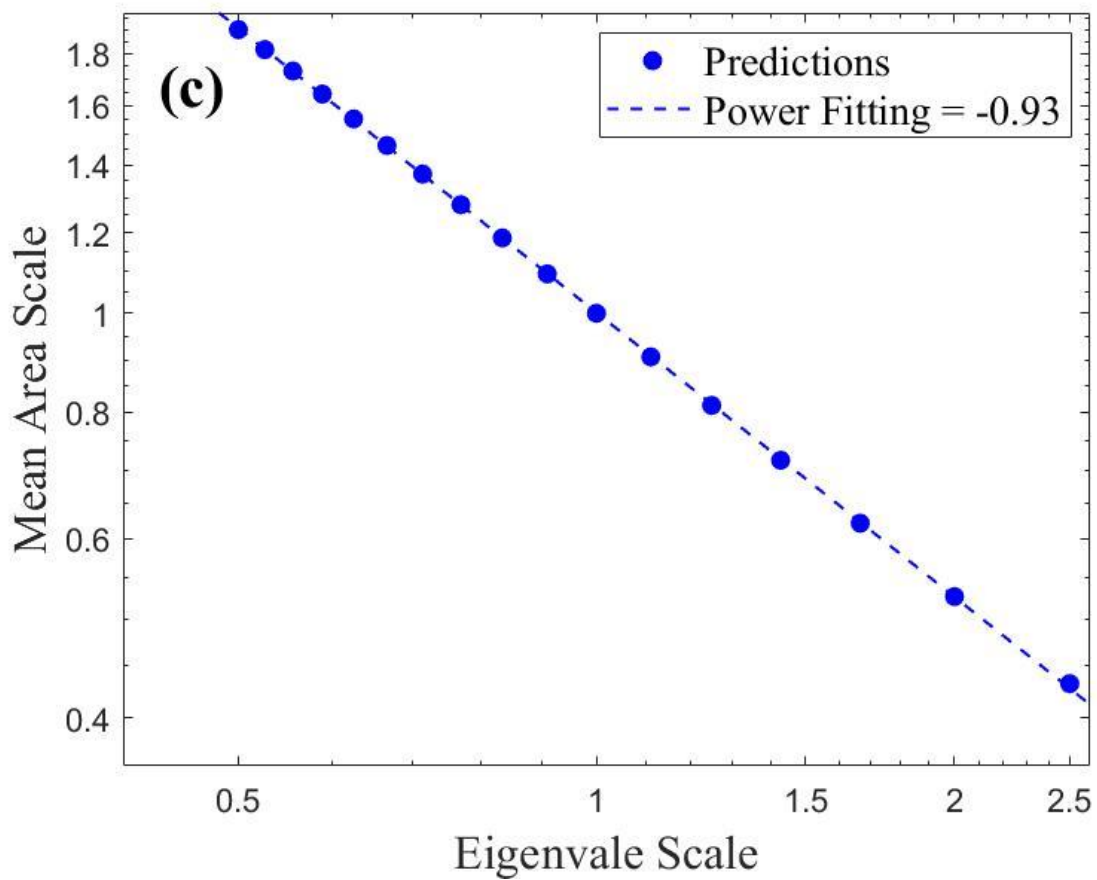


FIG 3. (a) Examples of the scaling behavior of the the predicted area. (b) The same scaling law holds even for poor predictions. (c) The predicted area as a function of the scaling factor. The fitted power-law (dashed line) has exponent of -0.93 .

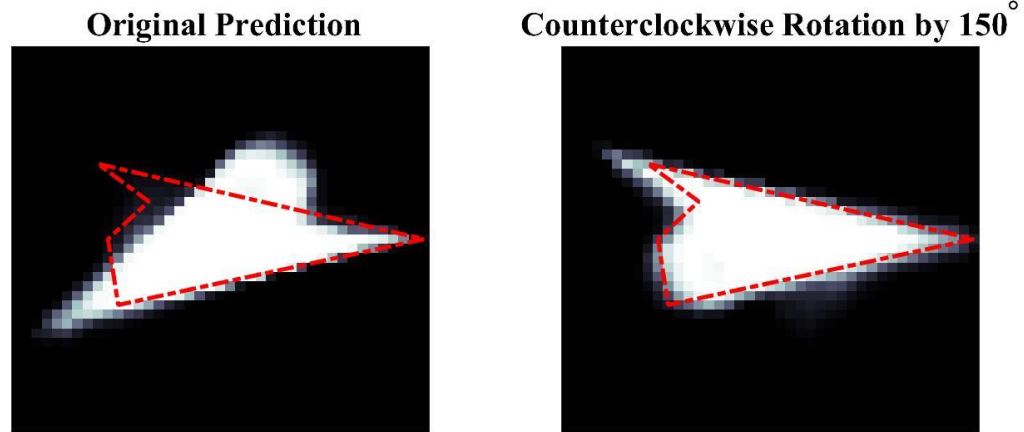


FIG 4. The DNN restores rotational symmetry beyond the limitations set by the square lattice. The true ground is displayed in red for comparison.

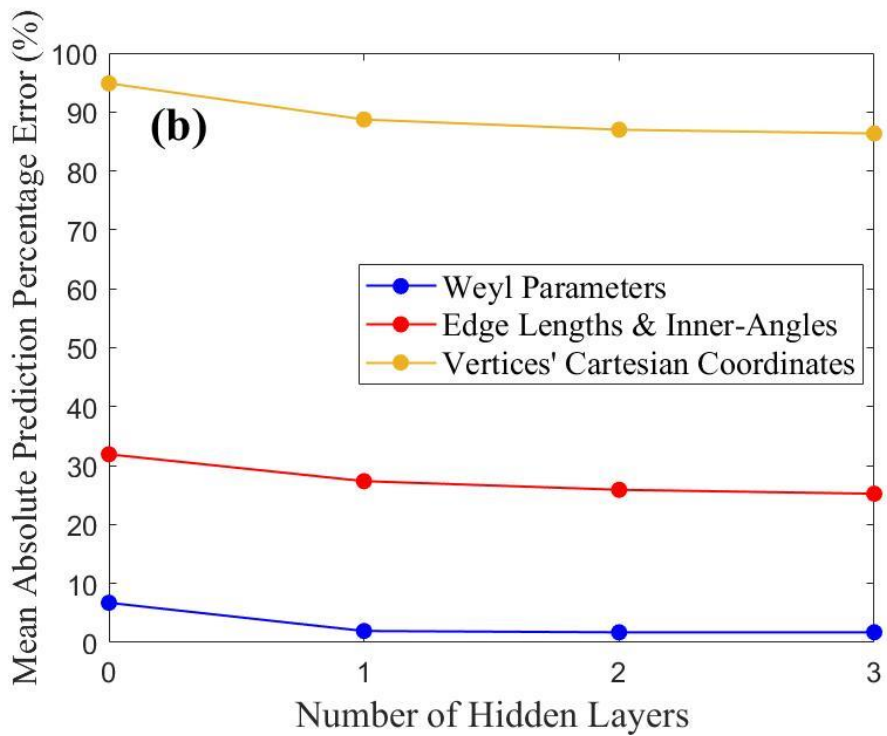
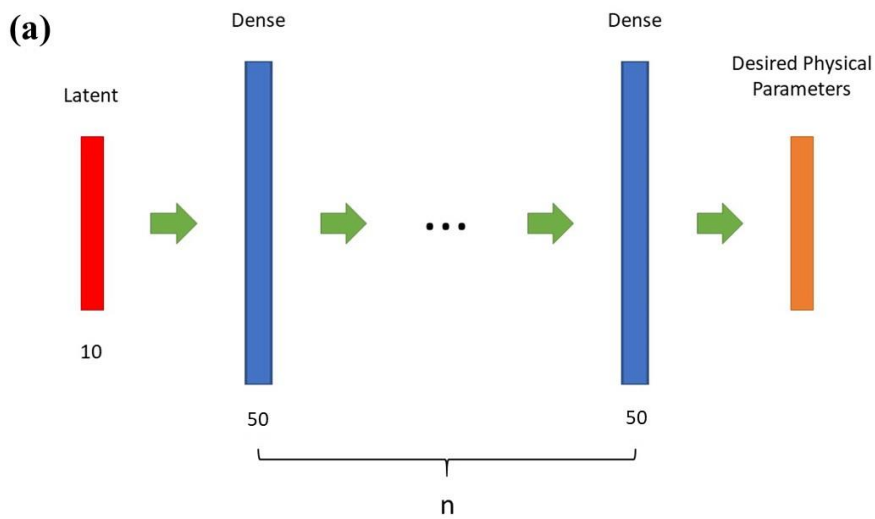


FIG 5. **(a)** The small network used to analyze the latent space. The latent values are injected into n consecutive hidden dense layers before the desired output parameters. **(b)** The mean absolute percentage error of predictions from the small network decreases as the number of hidden layers increases. Three types of parameters are taken into consideration: Weyl's parameters (blue), the edge lengths and inner-angles (red), and the Cartesian coordinates of vertices (yellow).

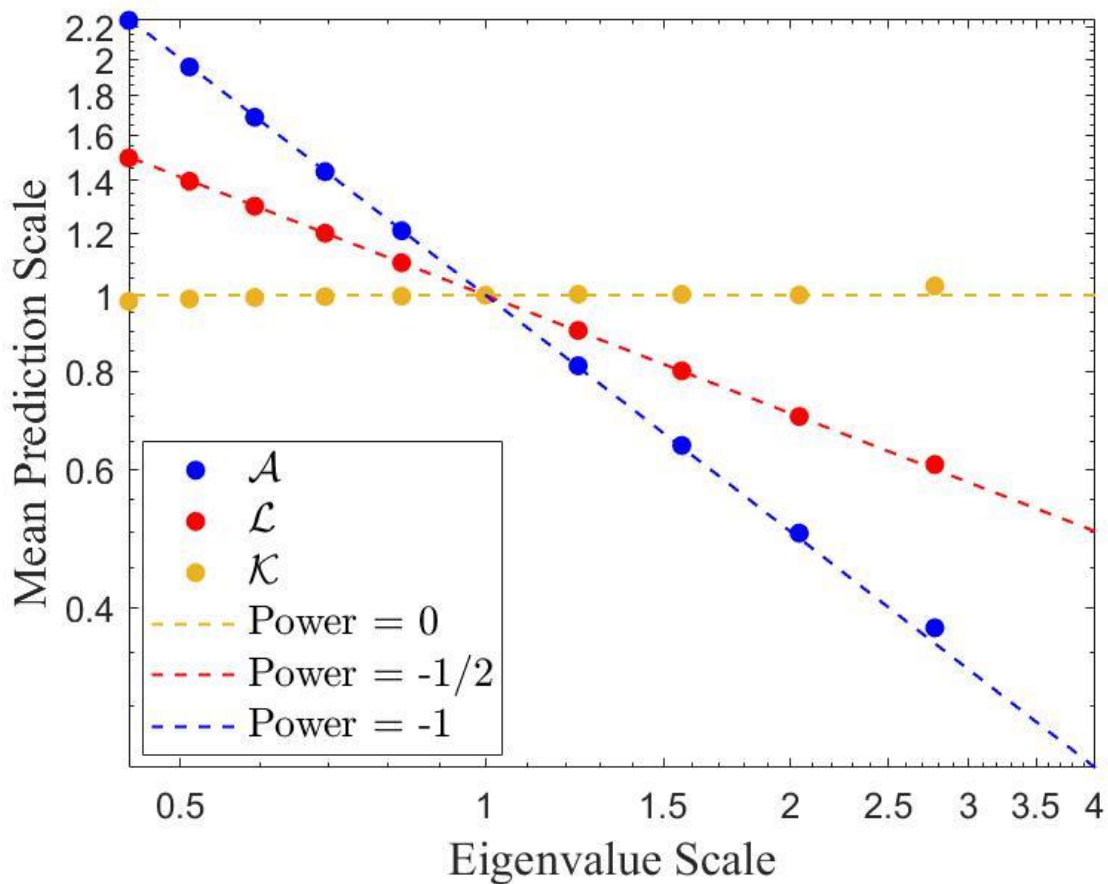


FIG 6. Scaling behavior of predicted Weyl's parameters (area, red dots; perimeter, blue dots; sum of angles, yellow dots) obtained using the small network with one hidden layer. The dashed lines indicate the ideal scaling laws. The test set contained 10,074 samples that remained within the training range for all scaling factors S shown.

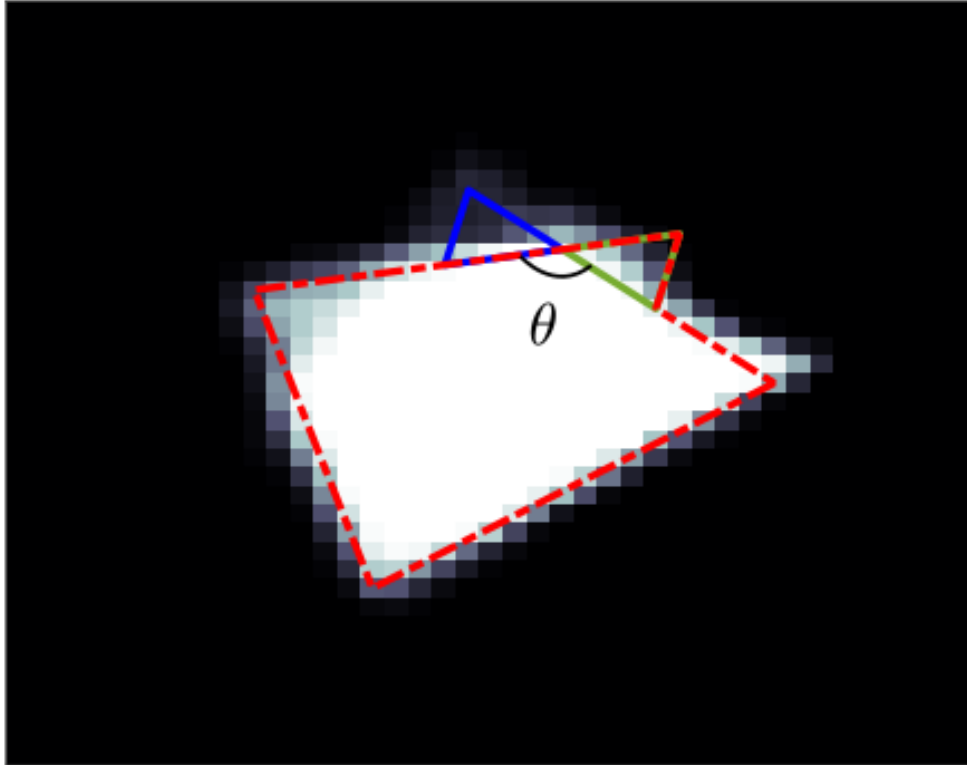


Fig 7. An expanded view of the “average” prediction introduced in Fig 2. The prediction has been rotated counterclockwise by 5° for maximal agreement with the ground truth (red box). The blue triangle is the reflection of the green triangle with respect to the bisector of the angle θ .

Citation

- [1] M. Kac, *Can One Hear the Shape of a Drum?*, Am. Math. Mon. **73**, 1 (1966).
- [2] C. Gordon, D. L. Webb, and S. Wolpert, *One Cannot Hear the Shape of a Drum*, Bull. Am. Math. Soc. **27**, 134 (1992).
- [3] O. Giraud and K. Thas, *Hearing Shapes of Drums: Mathematical and Physical Aspects of Isospectrality*, Rev. Mod. Phys. **82**, 2213 (2010).
- [4] M. Panine and A. Kempf, *Towards Spectral Geometric Methods for Euclidean Quantum Gravity*, Phys. Rev. D **93**, 084033 (2016).
- [5] S. Zelditch, *SPECTRAL DETERMINATION OF ANALYTIC BI-AXISYMMETRIC PLANE DOMAINS*, Math. Res. Lett. **6**, 457 (1999).
- [6] S. Zelditch, *Spectral Determination of Analytic Bi-Axisymmetric Plane Domains*, Geom. Funct. Anal. GAFA **10**, 628 (2000).
- [7] A. Iantchenko, J. Sjostrand, and M. Zworski, *Birkhoff Normal Forms in Semi-Classical Inverse Problems*, Math. Res. Lett. **9**, 337 (2002).
- [8] S. Zelditch, *Inverse Spectral Problem for Analytic Domains I: Balian-Bloch Trace Formula*, Commun. Math. Phys. **248**, 357 (2004).
- [9] S. Zelditch, *Inverse Resonance Problem for \mathbb{Z}_2 -Symmetric Analytic Obstacles in the Plane*, in *Geometric Methods in Inverse Problems and PDE Control*, edited by C. B. Croke, M. S. Vogelius, G. Uhlmann, and I. Lasiecka (Springer, New York, NY, 2004), pp. 289–321.
- [10] S. Zelditch, *Inverse Spectral Problem for Analytic Domains, II: \mathbb{Z}_2 -Symmetric Domains*, Ann. Math. **170**, 205 (2009).
- [11] D. Aasen, T. Bhamre, and A. Kempf, *Shape from Sound: Toward New Tools for Quantum Gravity*, Phys. Rev. Lett. **110**, 121301 (2013).
- [12] L. Cosmo, M. Panine, A. Rampini, M. Ovsjanikov, M. M. Bronstein, and R. Rodola, *Isospectralization, or How to Hear Shape, Style, and Correspondence*, in *2019 IEEE/CVF Conference on Computer Vision and Pattern Recognition (CVPR)* (IEEE, Long Beach, CA, USA, 2019), pp. 7521–7530.
- [13] T. Christensen, C. Loh, S. Picek, D. Jakobović, L. Jing, S. Fisher, V. Ceperic, J. D. Joannopoulos, and M. Soljačić, *Predictive and Generative Machine Learning Models for Photonic Crystals*, Nanophotonics **9**, 4183 (2020).
- [14] N. Borodinov, S. Neumayer, S. V. Kalinin, O. S. Ovchinnikova, R. K. Vasudevan, and S. Jesse, *Deep Neural Networks for Understanding Noisy Data Applied to Physical Property Extraction in Scanning Probe Microscopy*, Npj Comput. Mater. **5**, 1 (2019).
- [15] X. Chen, R. Ren, and M. Liu, *Validity of Machine Learning in the Quantitative Analysis of Complex Scanning Near-Field Optical Microscopy Signals Using Simulated Data*, Phys. Rev. Appl. **15**, 014001 (2021).

- [16] E. P. L. van Nieuwenburg, Y.-H. Liu, and S. D. Huber, *Learning Phase Transitions by Confusion*, Nat. Phys. **13**, 435 (2017).
- [17] J. Carrasquilla and R. G. Melko, *Machine Learning Phases of Matter*, Nat. Phys. **13**, 431 (2017).
- [18] X.-Y. Dong, F. Pollmann, and X.-F. Zhang, *Machine Learning of Quantum Phase Transitions*, Phys. Rev. B **99**, 121104 (2019).
- [19] P. Baldi, P. Sadowski, and D. Whiteson, *Searching for Exotic Particles in High-Energy Physics with Deep Learning*, Nat. Commun. **5**, 1 (2014).
- [20] P. Baldi, P. Sadowski, and D. Whiteson, *Enhanced Higgs Boson to $\tau^+\tau^-$ Search with Deep Learning*, Phys. Rev. Lett. **114**, 111801 (2015).
- [21] D. Guest, J. Collado, P. Baldi, S.-C. Hsu, G. Urban, and D. Whiteson, *Jet Flavor Classification in High-Energy Physics with Deep Neural Networks*, Phys. Rev. D **94**, 112002 (2016).
- [22] J. Wu, C. Zhang, T. Xue, B. Freeman, and J. Tenenbaum, *Learning a Probabilistic Latent Space of Object Shapes via 3D Generative-Adversarial Modeling*, in *Advances in Neural Information Processing Systems*, Vol. 29 (Curran Associates, Inc., 2016).
- [23] T. Aumentado-Armstrong, S. Tsogkas, A. Jepson, and S. Dickinson, *Geometric Disentanglement for Generative Latent Shape Models*, in *2019 IEEE/CVF International Conference on Computer Vision (ICCV)* (2019), pp. 8180–8189.
- [24] G. Pavlakos, V. Choutas, N. Ghorbani, T. Bolkart, A. A. Osman, D. Tzionas, and M. J. Black, *Expressive Body Capture: 3D Hands, Face, and Body From a Single Image*, in *2019 IEEE/CVF Conference on Computer Vision and Pattern Recognition (CVPR)* (IEEE, Long Beach, CA, USA, 2019), pp. 10967–10977.
- [25] A. Sinha, A. Unmesh, Q. Huang, and K. Ramani, *SurfNet: Generating 3D Shape Surfaces Using Deep Residual Networks*, in *2017 IEEE Conference on Computer Vision and Pattern Recognition (CVPR)* (IEEE, Honolulu, HI, 2017), pp. 791–800.
- [26] S. Reed, Z. Akata, X. Yan, L. Logeswaran, B. Schiele, and H. Lee, *Generative Adversarial Text to Image Synthesis*, in *International Conference on Machine Learning* (PMLR, 2016), pp. 1060–1069.
- [27] H. Zhang, T. Xu, H. Li, S. Zhang, X. Wang, X. Huang, and D. N. Metaxas, *StackGAN++: Realistic Image Synthesis with Stacked Generative Adversarial Networks*, IEEE Trans. Pattern Anal. Mach. Intell. **41**, 1947 (2019).
- [28] A. El-Nouby, S. Sharma, H. Schulz, R. D. Hjelm, L. E. Asri, S. E. Kahou, Y. Bengio, and G. Taylor, *Tell, Draw, and Repeat: Generating and Modifying Images Based on Continual Linguistic Instruction*, in *2019 IEEE/CVF International Conference on Computer Vision (ICCV)* (IEEE, Seoul, Korea (South), 2019), pp. 10303–10311.
- [29] K. Kottmann, P. Huembeli, M. Lewenstein, and A. Acín, *Unsupervised Phase Discovery with Deep Anomaly Detection*, Phys. Rev. Lett. **125**, 170603 (2020).
- [30] A. Rocchetto, E. Grant, S. Strelchuk, G. Carleo, and S. Severini, *Learning Hard Quantum Distributions with Variational Autoencoders*, Npj Quantum Inf. **4**, 1 (2018).

- [31] B. Lusch, J. N. Kutz, and S. L. Brunton, *Deep Learning for Universal Linear Embeddings of Nonlinear Dynamics*, Nat. Commun. **9**, 4950 (2018).
- [32] N. Takeishi, Y. Kawahara, and T. Yairi, *Learning Koopman Invariant Subspaces for Dynamic Mode Decomposition*, in *Advances in Neural Information Processing Systems*, Vol. 30 (Curran Associates, Inc., 2017).
- [33] S. E. Otto and C. W. Rowley, *Linearly Recurrent Autoencoder Networks for Learning Dynamics*, SIAM J. Appl. Dyn. Syst. **18**, 558 (2019).
- [34] R. Iten, T. Metger, H. Wilming, L. del Rio, and R. Renner, *Discovering Physical Concepts with Neural Networks*, Phys. Rev. Lett. **124**, 010508 (2020).
- [35] D. Zheng, V. Luo, J. Wu, and J. B. Tenenbaum, *Unsupervised Learning of Latent Physical Properties Using Perception-Prediction Networks*, ArXiv180709244 Cs Stat (2018).
- [36] S. Hochreiter and J. Schmidhuber, *Long Short-Term Memory*, Neural Comput. **9**, 1735 (1997).
- [37] A. L. Maas, A. Y. Hannun, and A. Y. Ng, *Rectifier Nonlinearities Improve Neural Network Acoustic Models*, in *ICML*, Vol. 30 (2013).
- [38] H. Weyl, *Ueber die asymptotische Verteilung der Eigenwerte*, Nachrichten Von Ges. Wiss. Zu Gött. Math.-Phys. Kl. **1911**, 110 (1911).
- [39] K. Stewartson and R. T. Waechter, *On Hearing the Shape of a Drum: Further Results*, Math. Proc. Camb. Philos. Soc. **69**, 353 (1971).
- [40] K. Hornik, M. Stinchcombe, and H. White, *Multilayer Feedforward Networks Are Universal Approximators*, Neural Netw. **2**, 359 (1989).
- [41] L. V. Brown, M. Davanco, Z. Sun, A. Kretinin, Y. Chen, J. R. Matson, I. Vurgaftman, N. Sharac, A. J. Giles, M. M. Fogler, T. Taniguchi, K. Watanabe, K. S. Novoselov, S. A. Maier, A. Centrone, and J. D. Caldwell, *Nanoscale Mapping and Spectroscopy of Nonradiative Hyperbolic Modes in Hexagonal Boron Nitride Nanostructures*, Nano Lett. **18**, 1628 (2018).
- [42] R. Marin, A. Rampini, U. Castellani, E. Rodolà, M. Ovsjanikov, and S. Melzi, *Spectral Shape Recovery and Analysis Via Data-Driven Connections*, Int. J. Comput. Vis. **129**, 2745 (2021).